Bloch-Wave Phase Matching of High Harmonic Generation in Solids

Liang Li[1,2] Yuntian Zhang,[1] Jiapeng Li,[1] Pengfei Lan,[1,2,*] and Peixiang Lu[1,2,†]

[1]*Wuhan National Laboratory for Optoelectronics and School of Physics,*
Huazhong University of Science and Technology, Wuhan 430074, China
[2]*Hubei Optical Fundamental Research Center, Wuhan 430074, China*

There has been a longstanding doubt that the conversion efficiency of high harmonics in solids is much lower than expected at such a high level of electron density. To address this issue, we revisit the dynamical process of high harmonic generation (HHG) in solids in terms of wavelet interference. We find that the constructive interference among the wavelets has intrinsic consistency with the phase matching of coupled waves in nonlinear optics, which we call Bloch-wave phase matching. Our analysis indicates that most of the wavelets are out of phase and coherently canceled out during the solid HHG process, leading to only a small fraction of excited electrons effectively contributing to HHG. Consequently, the conversion from the excited electron to HHG is fairly low. Moreover, a Bloch-wave phase-matching scheme is proposed and a nearly 3 orders of magnitude enhancement of solid HHG can be achieved by engineering the crystal structures. Our Letter addresses a longstanding doubt and provides a novel idea and theoretical guidance for realizing efficient all-solid-state tabletop ultraviolet light sources.

High harmonic generation (HHG) is an extremely non-linear optical process in which the radiated photon frequency can reach many times that of the driving laser [1–4]. By synthesizing HHG signals in a wide spectral range, ultrashort attosecond pulses can be obtained [5–10]. The HHG has laid the foundation for attosecond science and a series of attosecond techniques based on HHG has been developed for studying the ultrafast dynamical processes in atoms and molecules at the electron scale [11–18].

Currently, one of the critical problems limiting the application of attosecond light sources is the difficulty of achieving sufficient conversion efficiency. In recent years, HHG has been extended to solid materials [19,20], which is observed in a variety of material systems from traditional wide band gap dielectrics to emerging novel materials [21–26]. Unlike the sparse atoms or molecules in gases, the atomic structure in solid systems is much denser (3–6 orders of magnitude higher than that in gases). Thus, a much greater number of electrons can be excited in a unit volume, which provides the possibility for efficient conversion of HHG. Moreover, the laser intensity required to generate HHG in solids ($\sim$1 TW/cm^2) is much lower than that in gases ($\sim$100 TW/cm^2), which allows one to use a driving laser with higher repetition rate and average power. Besides, recent results have shown that the beam properties of the generated high harmonics can be manipulated using nanostructured surfaces, or metasurfaces [27–29]. Because

of these advantages, solid-state HHG is emerging as a promising way to obtain compact high-efficiency extreme-ultraviolet (XUV) light sources [19,20,30]. However, present experimental results show that the conversion efficiency of the solid HHG [21,31–33] is still at a similar level compared to that in gases [34,35]. Some schemes have been demonstrated to enhance the harmonic yield in solids by resonant effects [36,37] or exciting more electrons [38]. Nevertheless, the very low conversion of solid-state HHG at such a high level of electron density remains a long-standing doubt, which limits the development of all-solid-state tabletop XUV light sources.

In this Letter, we investigate the HHG emission in solids from the Bloch-wave phase-matching perspective, where the HHG process is dissected in terms of the interference of Bloch wavelets in a parameter space. Our results show that the relative phase of wavelets in a regular crystal varies over a wide range, thus leading to the phase mismatch among these wavelets. As a result, the effective number of electrons contributing to HHG only accounts for a small fraction of the excited electrons. This leads to a much lower yield of harmonics in solids than that of gases already in the microscopic response, which can address why the conversion efficiency of HHG in solids is much lower than expected. To enhance the HHG, we show a demo scheme for optimizing the Bloch-wave phase matching by using a structured crystal. Atomic-level structure engineering in crystals significantly modulates electron motion so as the relative phases among different wavelets, and nearly 3 orders of magnitude enhancement of HHG can be achieved under optimal phase-matching conditions.

(a)

(b)
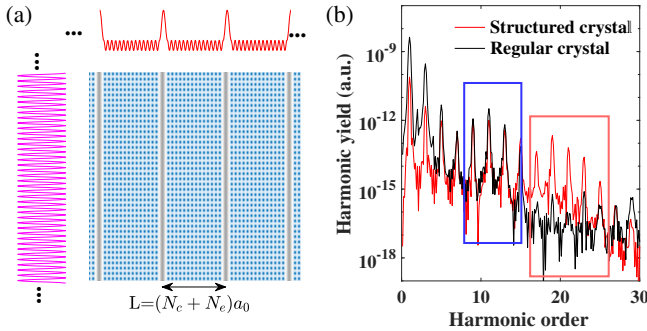
FIG. 1. (a) Schematic diagrams of the structured crystal. Gray areas indicate the etched regions. The red and purple lines show the intercepts of the effective potential along the x and y axes, respectively. (b) HHG spectra for a regular crystal and a structured crystal. The blue and red boxes mark two areas with different typical phenomena.

We first show the derivation of the Bloch-wave phase-matching perspective and how it works in a generalized parameter space. Without loss of generality, we model the solid HHG following the framework in Refs. [39,40]. The harmonic yield can be rewritten as accumulation of Bloch wavelets in parameter space (details are shown in Sec. A of Supplemental Material [41]),

$$Y(\Omega) \propto \left| \sum_{\mathbf{k}_l, \mathbf{r}', t_r} f(\mathbf{k}_l, \mathbf{r}', t_r) G(\mathbf{k}_l, \mathbf{r}', t_r; \Omega) e^{-i\varphi(\mathbf{k}_l, r', t_r; \Omega)} \right|^2. \quad (1)$$

In this form, $f(\mathbf{k}_l, \mathbf{r}', t_r)$ is the weight of the Bloch wavelets and $G(\mathbf{k}_l, \mathbf{r}', t_r; \Omega) e^{-i\varphi[\mathbf{k}_l, \mathbf{r}', t_r; \Omega]}$ is the contribution of a

single filtered wavelets in parameter space propagating from $\{k_l, \mathbf{r}', t_r\}$ to $\{\Omega\}$. The indexes indicate which electron $\{\mathbf{k}_l\}$ when $\{t_r\}$ and where $\{\mathbf{r}'\}$ emits the harmonic $\{\Omega\}$. The propagation phase $\varphi[\mathbf{k}_l, \mathbf{r}', t_r; \Omega]$ is gauge-independent, which is determined by the quantum paths of Bloch waves and the corresponding energy dispersion in the parameter space. The summation over t_r is the temporal interference mentioned in [42,43]. In this Letter, we only focus on the interference in coordinate and crystal-momentum space, i.e., $\{\mathbf{r}'\}$ and $\{\mathbf{k}_l\}$.

As in Eq. (1), the expression of HHG yield shows an intrinsically consistent form with the propagation of coupled waves in nonlinear optics [41,44], only with a change of propagation path from spatial space to a parameter space $\{\mathbf{k}_l, \mathbf{r}', t_r; \Omega\}$. This similarity allows us to use similar physical pictures and method to understand the solid HHG in analogy with the macroscopic phase matching in nonlinear optics. Thus, we call the constructive condition of harmonic emission as Bloch-wave phase matching, which is essentially interference between HHG contributed by different Bloch waves, and the phase-matching condition gives $\Delta\varphi[\mathbf{k}_l, \mathbf{r}', t_r; \Omega] = 0$.

To demonstrate the role of Bloch-wave phase matching in solid HHG, we take a two-dimensional (2D) model system with a square lattice structure as an example. For comparison, we also consider a structured crystal, where the interaction among atoms is limited by engineering the crystal structures, and thus the electron motion and phase matching can be modulated. We model these crystals using a periodic effective potential,

$$V_{\text{eff}}(x, y) = \begin{cases} V_h \sin^2\{[(x + N_c a_0/2)]/[N_e a_0]\pi\}, x \in [-L/2, -N_c a_0/2) \\ -\frac{V_0}{4}[1 - \cos(2\pi x/a_0)][1 - \cos(2\pi y/a_0)], x \in [-N_c a_0/2, N_c a_0/2] \\ V_h \sin^2\{[(x - N_c a_0/2)]/[N_e a_0]\pi\}, x \in (N_c a_0/2, L/2), \end{cases} \quad (2)$$

where $L = (N_c + N_e)a_0$ with N_c and N_e is the number of consecutive and etching atoms in a single cell along the x axis. a_0 is the lattice constant. Schematic diagrams (crystal lattice) and intercepts of the effective potential in different directions (red and purple lines) are shown in Fig. 1(a). For a regular crystal ($N_c = 1$ and $N_e = 0$), we set $a_0 = 6$ atom units (a.u.) and $V_0 = 0.4$ a.u. to mimic the band gap 3.2 eV for a ZnO crystal. The influence of the etching atoms is modeled by a barrier potential with $V_h = 1.2$ a.u. Note that our Letter focuses on some general physics rather than specific materials. The model potential mimics the general property of semiconductors with a given band gap, which has been used for studying solid HHG [45–47].

The interaction of the crystal with laser fields is simulated by solving the time-dependent Schrödinger

equation with accelerated Bloch basis [39],

$$i\partial_t \alpha_{n,\mathbf{k}}(t) = E_n[\mathbf{k} + \mathbf{A}(t)]\alpha_{n,\mathbf{k}}(t) + \mathbf{F}(t) \cdot \sum_m \mathbf{d}_{nm}\alpha_{m,\mathbf{k}}(t). \quad (3)$$

$\mathbf{F}(t) = -\{[d\mathbf{A}(t)]/[dt]\}$ is the electric field. The energy band $E_n(\mathbf{k})$ and the dipole momenta $\mathbf{d}_{nm}(k) = \langle u_{n,\mathbf{k}}|i\nabla_{\mathbf{k}}|u_{m,\mathbf{k}}\rangle$ are determined by the eigenequations with the periodic effective potential $V_{\text{eff}}(x, y)$, where $|u_{m,\mathbf{k}}\rangle$ is the periodic part of the Bloch function. The HHG spectra are obtained by $I(\omega) = \omega^2|\text{FFT}[\int_{\text{BZ}}\langle\Psi_{\mathbf{k}}(t)|\mathbf{p} + \mathbf{A}(t)|\Psi_{\mathbf{k}}(t)\rangle d\mathbf{k}]|^2$. A laser pulse linearly polarized along the x axis is applied with a trapezoidal envelope containing two optical-cycles rising, four optical-cycles flat, and a two

optical-cycles falling edges. The wavelength and intensity are set to be 2000 nm and 0.5 TW/cm^2. In Fig. 1(b), we plot the harmonic spectra for a regular crystal and a structured crystal ($N_c = 14$, and $N_e = 2$). One can see that the yield of low-energy harmonics (the 9–15th harmonics marked by the blue box) in the structure crystal is comparable to or even lower than those in the regular crystal. In contrast, the yield of the high-energy harmonics (the 17–25th harmonics marked by the red box) is enhanced by about 3 orders of magnitude in the structured crystals. Similar enhancement also can be obtained for other laser wavelengths and intensities (see Sec. C in Supplemental Material [41]).

We choose the 9th (low-energy region) and 19th harmonics (high-energy region) as representatives to analyze the phase-matching process. We first focus on the wavelets with different crystal momenta,

$$\mathbf{J}_{k_l}(\Omega) = \int_0^{2\pi/L} \int_0^{2\pi/L} \int_{-\infty}^{+\infty} W_{\delta_k}(k_l, k_x)\langle\Psi_\mathbf{k}(t)|\mathbf{p} + \mathbf{A}(t)|\Psi_\mathbf{k}(t)\rangle e^{i\Omega t}\mathrm{d}t\mathrm{d}k_y\mathrm{d}k_x. \tag{4}$$

Here, we use a window $W_{\delta_k}(k_l, k_x)$ with $\delta_k = [(2\pi/L)/(20)]$. We also plot the 2D band structures and wavelet distribution and found little influence of the Bloch-wave phase matching along the k_y direction. Thus, the change of the yield is dominant by the structure along k_x direction and we focus on the discussion along the k_x direction.

To analyze the phase-matching process in crystal-momentum space, we plot the individual k-wavelet contribution $C_{k_l}(\Omega) = |\mathbf{J}_{k_l}(\Omega)|^2$ and the accumulated harmonic yields $Y_{k_l}(\Omega) = |\int_0^{k_l} \int_0^{2\pi/L} \int_{-\infty}^{+\infty} \langle\Psi_\mathbf{k}(t)|\mathbf{p} + \mathbf{A}(t)|\Psi_\mathbf{k}(t)\rangle e^{i\Omega t}\mathrm{d}t\mathrm{d}k_y\mathrm{d}k_x|^2$ in Figs. 2(c)–2(f). For a regular crystal, one can see that the individual k-wavelet distribution (dashed blue lines) shows a peak near $k_l = 0.5[(2\pi)/(a_0)]$ for the 9th harmonic and $k_l = (0.5 \pm 0.34)[(2\pi)/(a_0)]$ for the 19th harmonic. These distributions can be explained by considering different preacceleration processes of the excited electrons contributing to the low- and high-energy region [48]. Moreover, as shown in Figs. 2(c) and 2(e), the phase of the wavelet contributing to the 9th and 19th harmonics (solid red lines) both continuously oscillate from -0.5π to 0.5π. In this case, the harmonics contributed by the wavelets with different crystal momenta are repeatedly constructive and destructive interference. Thus, the accumulated harmonic yields show a strong oscillation, and the final harmonic yield is limited (solid blue lines).

Using the concept of Bloch-wave phase matching, one can understand the difference between the microscopic dynamics of HHG from gases and solids. In the gas medium, the spacing between atoms (or molecules) is so large that the coupling between them can be neglected. In this case, all electrons are initially located at the same ground state and the generated harmonics have the same phase in the microscopic response. Thus, the contributions from different atoms are constructively interfered with each other if one ignores the macroscopic propagation effect (or assuming that they are perfectly phase-matched), and then the conversion efficiency of HHG is proportional to the number of atoms. As a comparison, the coupling between different atoms forms energy bands in solid systems, and the contributions of different electron states are no longer independent with each other. In this case, the electron dynamics is described by the collective mode, e.g., Bloch waves, and their interference results in the harmonic yield as in Eq. (1). Different Bloch wavelets may experience different quantum paths and accumulate phases in a wide range [Figs. 2(c) and 2(e)]. Thus, the harmonic yields among different Bloch wavelets are destructively interfered with each other. This leads to a much lower yield of harmonics in solids than that of gases already in the microscopic response. This effect addresses the long-standing doubt as to why solids do not exhibit high conversion efficiency although the concentration of carriers is much higher than atomic gases.
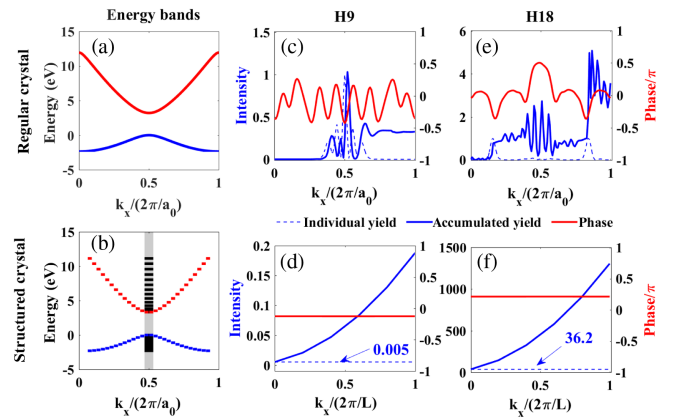
FIG. 2. (a), (b) The band structures of a regular crystal and a structured crystal. The gray area marks the first Brillouin zone (BZ) for the structured crystal. (c)–(f) The individual wavelet contributions (dashed blue lines), and accumulated harmonic yields (solid blue lines) for the 9th (low-energy region) and 19th (high-energy region) harmonics in the first BZ. The red lines show the phases of each wavelet. For each harmonic, the maximum individual harmonic yield for a regular crystal is normalized to 1, and other lines for harmonic yields are shown as its relative value.

The above discussion indicates that one can realize the Bloch-wave phase matching by modulating the quantum paths or the energy dispersion along the paths. To show this, we provide a demo scheme for optimizing the Bloch-wave phase matching by using a structured crystal. As shown in Figs. 2(e) and 2(f), for both the 9th and the 19th harmonics, all the individual k wavelets have almost the same phases and amplitudes. Thus, the wavelets are phase-matched, and their contributions are constructive with each other. This result can be understood by the modulation of the electron bands as shown in Figs. 2(a) and 2(b). For a regular crystal, the electron energy band has a continuously bent structure. The electrons with different crystal momenta will go through different quantum paths and the phases accumulated from them have large differences. In contrast, the energy bands of structured crystal are folded into a narrow region and each band is divided into 14 sub-bands with almost flat structure. The Bloch wavelets with different k can move on and jump between these bands, and different k wavelets accumulate phases nearly the same considering the flat band structure. In this case, all the wavelets are coherently constructive with each other and the accumulated harmonic yield shows a parabolic growth [see solid blue lines in Figs. 2(d) and 2(f)].

Besides the phase matching, the amplitude of the individual k wavelet also influences the accumulated harmonic yield. As shown in Fig. 2(d), the individual k-wavelet contribution (dashed blue line) in the structured crystal is much lower in the low-energy region (about 0.005) compared with the regular crystal. Therefore, the total harmonic yield is still slightly smaller in the low-energy region even though a good phase matching is satisfied.

FIG. 3. (a)–(d) The coordinate-wavelet contributions (blue lines with shadow) for the 9th (low-energy region) and 19th (high-energy region) harmonics. The red lines show the phases of each wavelet. For each harmonic, the maximum individual harmonic yield for a regular crystal is normalized to 1, and other lines for harmonic yields are shown as its relative value. (e)–(f) The time-space distribution of the 19th harmonic for a regular and a structured crystal with the maximum amplitude being normalized to 1 in both cases.

In contrast, the individual k-wavelet contribution [dashed blue line in Fig. 2(f)] is much higher in the high-energy region (about 32.6), and the total harmonic yield in the structured crystal is enhanced by almost 3 orders of magnitude.

The difference between the individual k-wavelet contributions in the low-energy and high-energy regions shown above can be understood by spatial interference. To show this influence, we further analyze wavelets in the coordinate space,

$$\mathbf{J}_{x'}^{k_x}(\Omega) = \int_0^{2\pi/L} \int_{-\infty}^{+\infty} \int_{\text{Cell}} W_{\delta_x}(x',x)\{\Psi_{k_x,k_y}^*(\mathbf{r},t)[\hat{\mathbf{p}}+\mathbf{A}(t)]\Psi_{k_x,k_y}(\mathbf{r},t)\}e^{i\Omega t}\mathrm{d}\mathbf{r}\mathrm{d}t\mathrm{d}k_y, \tag{5}$$

using a spatial window $W_{\delta_x}(x',x)$ with $\delta_x = (L/20)$. Then, one can obtain the coordinate-wavelet contribution $C_{x'}^{k_0} = |\mathbf{J}_{x'}^{k_0}|^2$, and the corresponding phase distribution. We focus our discussions on the dominant electron states, i.e., $k_x/K_{\max} = 0.5$ and 0.16 ($K_{\max} = 2\pi/a_0$ or $2\pi/L$ for a regular or structured crystal) for the 9th and 19th harmonics, respectively. As shown in Figs. 3(a)–3(d), the dashed blue lines with shadow show the coordinate-wavelet contributions and the solid red lines show the phase distributions. For the 9th harmonic, one can see that the coordinate-wavelet contributions for a regular crystal show a two-peak structure, and the phases change a little (less than 0.1π) near the peaks. However, for a structured crystal, the amplitude distribution of the wavelets spreads out and the maximum amplitude decreases to about 0.3. Besides, the phases also change from π to 0, i.e., the phase-matching condition is not maintained in the coordinate space. These factors result

in a lower contribution of a structured crystal as shown in Fig. 2(d). In contrast, for the 19th harmonic, the coordinate-wavelet contributions of a structured crystal are localized to the cell boundary, and the maximal amplitude is about 4.6 times higher than that of a regular crystal. Besides, the phases show a step change among π, 0.1π, and -0.5π, and some degree of constructive interference is still maintained. As a comparison, the coordinate-wavelet contributions of a regular crystal have four peaks but the neighboring two peaks with nearly π phase shift and almost cancel out with each other. Thus, a relatively higher amplitude is obtained for a structured crystal as shown in Fig. 2(f).

One can understand the dynamic processes behind the wavelet interference by analyzing the time-space distribution of harmonic radiation, which can be obtained by $Y_\Omega^{k_x}(x',t') = \Omega^2|\int_0^{[(2\pi)/L]} \int_{-\infty}^{+\infty} \int_{\text{Cell}} W_{\delta_x}(x',x)W_{\delta_t}(t',t)\{\Psi_{k_x,k_y}^*(\mathbf{r},t)[\hat{\mathbf{p}}+\mathbf{A}(t)]\Psi_{k_x,k_y}(\mathbf{r},t)\}e^{i\Omega t}\mathrm{d}\mathbf{r}\mathrm{d}t\mathrm{d}k_y|^2$. This distribution indicates
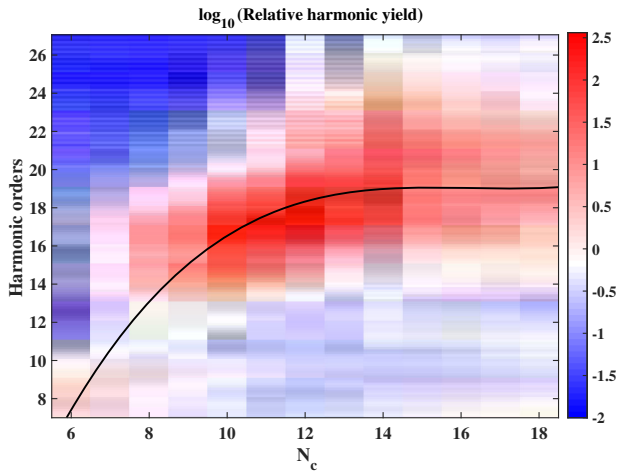
FIG. 4. The relative harmonic yield in structured crystals compared with that in a regular crystal. For clarity, we smooth the harmonic spectra, and the results are shown in a logarithmic scale. The black line is plotted to guide the eyes for the tendency.

when and where the high harmonics are radiated, intuitively visualizing the dynamics behind the HHG process. We show the dynamic distributions for the 19th harmonic of regular and structured crystals in Figs. 3(e) and 3(f). For a regular crystal, the harmonic radiations are dispersed throughout the cell and exhibit an overall rise and fall with time evolution. Such a collective behavior leads to a continuous phase variation of different wavelets, which makes it difficult to obtain a high harmonic conversion ratio. In contrast to this collective behavior, the harmonic radiations in a structured crystal are localized and move from one side to another every half-optical cycle. This more concentrated radiation behavior leads to a more efficient energy release, which explains phase matching among wavelets.

Building on the above results, we next demonstrate that one can modulate the Bloch-wave phase matching by changing the crystal structures. In Fig. 4, we plot the ratio of HHG yield between a structured crystal and a regular crystal with N_c changing from 6 to 18. The other parameters are kept the same parameters as those in Fig. 1. It is worth noting that the excitation of electrons for different structures is at the same level (near 1‰) within the parameters in our Letter, which excludes the effect of higher excitation of electrons. One can see that the phase-matched region can be modulated from lower to high harmonics (black line to guide the eyes) by increasing N_c. These results can be understood in terms of two aspects. On the one hand, optimal phase matching and localized enhancement can be achieved when the range of electron oscillations matches the width of the region between the etched atoms. Therefore, the optimal phase-matched harmonic order becomes higher with increasing N_c. On the other hand, as N_c further increases ($N_c > 14$), the influence of etched atoms becomes smaller and smaller, and the behavior of electrons asymptotically tends to that of a regular crystal, breaking the phase-matching conditions.

In summary, we derived the concept of Bloch-wave phase matching in a generalized parameter space. By analyzing the coordinate and crystal-momentum-space interference, we found that the wavelet contributions in a regular crystal are out of phase with each other, and only a small fraction of the excited electrons effectively contribute to the HHG. Our results address the longstanding doubt as to why the conversion efficiency is much lower than expected in solid HHG. Moreover, we propose a demo scheme to optimize the Bloch-wave phase matching by structure engineering, which can be realized by etching, doping, or synthesis techniques in experiments. Nearly 3 orders of magnitude of enhancement have been demonstrated in a structured crystal and the optimal phase-matching region can be modulated by changing the crystal structures. Looking forward, our scheme emphasizes the importance of Bloch-wave phase matching that depends on microscopic dynamics. It can be combined with other techniques that enhance the HHG via modulating the light propagation or electron injection [27–29,36–38]. This suggests a novel idea for achieving high-efficiency HHG and provides theoretical guidance for realized all-solid-state tabletop XUV light sources. Beyond these, one can expect to extend this perspective to other strong-field phenomena, e.g., strong-field ionization. This provides a new analytical method to intuitively resolve the electron dynamics behind different physical processes in strong fields.

[1] M. Ferray, A. L'Huillier, X. F. Li, L. A. Lompre, G. Mainfray, and C. Manus, J. Phys. B **21,** L31 (1988).

[2] A. McPherson, G. Gibson, H. Jara, U. Johann, T. S. Luk, I. A. McIntyre, K. Boyer, and C. K. Rhodes, J. Opt. Soc. Am. B **4,** 595 (1987).

[3] A. L'Huillier and P. Balcou, Phys. Rev. Lett. **70,** 774 (1993).

[4] J. J. Macklin, J. D. Kmetec, and C. L. Gordon, Phys. Rev. Lett. **70,** 766 (1993).

[5] P. Antoine, A. L'Huillier, and M. Lewenstein, Phys. Rev. Lett. **77,** 1234 (1996).

[6] P. M. Paul, E. S. Toma, P. Breger, G. Mullot, F. Augé, P. Balcou, H. G. Muller, and P. Agostini, Science **292,** 1689 (2001).

[7] M. Hentschel, R. Kienberger, C. Spielmann, G. A. Reider, N. Milosevic, T. Brabec, P. Corkum, U. Heinzmann, M. Drescher, and F. Krausz, Nature (London) **414,** 509 (2001).

[8] G. Sansone, L. Poletto, and M. Nisoli, Nat. Photonics **5,** 655 (2011).

[9] F. Calegari, M. Lucchini, M. Negro, C. Vozzi, L. Poletto, O. Svelto, S. De Silvestri, G. Sansone, S. Stagira, and M. Nisoli, J. Phys. B **45**, 074002 (2012).

[10] J. Li, X. Ren, Y. Yin, K. Zhao, A. Chew, Y. Cheng, E. Cunningham, Y. Wang, S. Hu, Y. Wu, M. Chini, and Z. Chang, Nat. Commun. **8**, 186 (2017).

[11] O. Smirnova, Y. Mairesse, S. Patchkovskii, N. Dudovich, D. Villeneuve, P. Corkum, and M. Y. Ivanov, Nature (London) **460**, 972 (2009).

[12] S. Haessler, J. Caillat, W. Boutu, C. Giovanetti-Teixeira, T. Ruchon, T. Auguste, Z. Diveki, P. Breger, A. Maquet, B. Carré, R. Taïeb, and P. Salières, Nat. Phys. **6**, 200 (2010).

[13] C. Vozzi, M. Negro, F. Calegari, G. Sansone, M. Nisoli, S. De Silvestri, and S. Stagira, Nat. Phys. **7**, 822 (2011).

[14] P. M. Kraus, B. Mignolet, D. Baykusheva, A. Rupenyan, L. Horný, E. F. Penka, G. Grassi, O. I. Tolstikhin, J. Schneider, F. Jensen, L. B. Madsen, A. D. Bandrauk, F. Remacle, and H. J. Wörner, Science **350**, 790 (2015).

[15] B. D. Bruner, H. Soifer, D. Shafir, V. Serbinenko, O. Smirnova, and N. Dudovich, J. Phys. B **48**, 174006 (2015).

[16] P. Lan, M. Ruhmann, L. He, C. Zhai, F. Wang, X. Zhu, Q. Zhang, Y. Zhou, M. Li, M. Lein, and P. Lu, Phys. Rev. Lett. **119**, 033201 (2017).

[17] L. He, S. Sun, P. Lan, Y. He, B. Wang, P. Wang, X. Zhu, L. Li, W. Cao, P. Lu, and C. D. Lin, Nat. Commun. **13**, 4595 (2022).

[18] A. Camper, A. Ferré, V. Blanchet, D. Descamps, N. Lin, S. Petit, R. Lucchese, P. Salières, T. Ruchon, and Y. Mairesse, Phys. Rev. Lett. **130**, 083201 (2023).

[19] S. Ghimire, A. D. DiChiara, E. Sistrunk, P. Agostini, L. F. DiMauro, and D. A. Reis, Nat. Phys. **7**, 138 (2011).

[20] S. Ghimire and D. A. Reis, Nat. Phys. **15**, 10 (2019).

[21] T. T. Luu, M. Garg, S. Y. Kruchinin, A. Moulet, M. T. Hassan, and E. Goulielmakis, Nature (London) **521**, 498 (2015).

[22] G. Ndabashimiye, S. Ghimire, M. Wu, D. A. Browne, K. J. Schafer, M. B. Gaarde, and D. A. Reis, Nature (London) **534**, 520 (2016).

[23] Y. S. You, D. A. Reis, and S. Ghimire, Nat. Phys. **13**, 345 (2016).

[24] H. Kim, S. Han, Y. W. Kim, S. Kim, and S.-W. Kim, ACS Photonics **4**, 1627 (2017).

[25] H. Liu, Y. Li, Y. S. You, S. Ghimire, T. F. Heinz, and D. A. Reis, Nat. Phys. **13**, 262 (2016).

[26] N. Yoshikawa, T. Tamaya, and K. Tanaka, Science **356**, 736 (2017).

[27] M. Sivis, M. Taucer, G. Vampa, K. Johnston, A. Staudte, A. Y. Naumov, D. M. Villeneuve, C. Ropers, and P. B. Corkum, Science **357**, 303 (2017).

[28] S. A. Jalil, K. M. Awan, I. A. Ali, S. Rashid, J. Baxter, A. Korobenko, G. Ernotte, A. Naumov, D. M. Villeneuve, A. Staudte, P. Berini, L. Ramunno, and G. Vampa, Optica **9**, 987 (2022).

[29] G. Zograf, K. Koshelev, A. Zalogina, V. Korolev, R. Hollinger, D.-Y. Choi, M. Zuerch, C. Spielmann, B. Luther-Davies, D. Kartashov, S. V. Makarov, S. S. Kruk, and Y. Kivshar, ACS Photonics **9**, 567 (2022).

[30] M. Garg, M. Zhan, T. T. Luu, H. Lakhotia, T. Klostermann, A. Guggenmos, and E. Goulielmakis, Nature (London) **538**, 359 (2016).

[31] S. Gholam-Mirzaei, J. Beetar, and M. Chini, Appl. Phys. Lett. **110** (2017).

[32] B. D. Bruner, A. J. Narovlansky-Uzan, T. Arusi-Parpar, G. Orenstein, A. Shonfeld, and N. Dudovich, J. Phys. B **54**, 154001 (2021).

[33] M. R. Shcherbakov, H. Zhang, M. Tripepi, G. Sartorello, N. Talisa, A. AlShafey, Z. Fan, J. Twardowski, L. A. Krivitsky, A. I. Kuznetsov, E. Chowdhury, and G. Shvets, Nat. Commun. **12** (2021).

[34] A. Cabasse, G. Machinet, A. Dubrouil, E. Cormier, and E. Constant, Opt. Lett. **37**, 4618 (2012).

[35] B. Xue, Y. Tamaru, Y. Fu, H. Yuan, P. Lan, O. D. Mücke, A. Suda, K. Midorikawa, and E. J. Takahashi, Sci. Adv. **6**, eaay2802 (2020).

[36] H. Liu, C. Guo, G. Vampa, J. L. Zhang, T. Sarmiento, M. Xiao, P. H. Bucksbaum, J. Vučković, S. Fan, and D. A. Reis, Nat. Phys. **14**, 1006 (2018).

[37] P. Peterka, Z. šobáň, F. Trojánek, P. Malý, and M. Kozák, Opt. Express **31**, 6401 (2023).

[38] S. Xu, J. Yu, C. Ye, H. Zhang, Z. Wang, and J. Hu, Appl. Phys. Lett. **122**, 182105 (2023).

[39] V. S. Yakovlev, S. Y. Kruchinin, T. Paasch-Colberg, M. I. Stockman, and F. Krausz, *Ultrafast Control of Strong-FieldElectron Dynamics in Solids* (Springer International Publishing, Switzerland, 2016).

[40] L. Li, P. Lan, X. Zhu, and P. Lu, Rep. Prog. Phys. **86**, 116401 (2023).

[41] See Supplemental Material at http://link.aps.org/supplemental/10.1103/PhysRevLett.133.116902 for a detailed derivation of our theory and additional complementary discussions.

[42] Y. S. You, M. Wu, Y. Yin, A. Chew, X. Ren, S. Gholam-Mirzaei, D. A. Browne, M. Chini, Z. Chang, K. J. Schafer, M. B. Gaarde, and S. Ghimire, Opt. Lett. **42**, 1816 (2017).

[43] L. Li, P. Lan, L. He, W. Cao, Q. Zhang, and P. Lu, Phys. Rev. Lett. **124**, 157403 (2020).

[44] R. W. Boyd, *Nonlinear Optics* (Academic Press, Boston, MA, 2008).

[45] M. Wu, S. Ghimire, D. A. Reis, K. J. Schafer, and M. B. Gaarde, Phys. Rev. A **91**, 043839 (2015).

[46] J.-Z. Jin, X.-R. Xiao, H. Liang, M.-X. Wang, S.-G. Chen, Q. Gong, and L.-Y. Peng, Phys. Rev. A **97**, 043420 (2018).

[47] Y. Lang, Z. Peng, J. Liu, Z. Zhao, and S. Ghimire, Phys. Rev. Lett. **129**, 167402 (2022).

[48] L. Li, P. Lan, X. Zhu, T. Huang, Q. Zhang, M. Lein, and P. Lu, Phys. Rev. Lett. **122**, 193901 (2019).